CI&CEQ
Chemical Industry & Chemical Engineering Quarterly

Available on line at
Association of the Chemical Engineers of Serbia *AChE*
www.ache.org.rs/CICEQ

Chem. Ind. Chem. Eng. Q. 27 (4) 329–340 (2021) CI&CEQ

J.N.M. BATISTA
R. BÉTTEGA

Federal University of São Carlos, Department of Chemical Engineering, SP, Brazil

SCIENTIFIC PAPER

UDC 633.17:66:544:519.87

EVALUATION OF DIFFERENT MATHEMATICAL MODELS IN THE CFD-DEM SIMULATION OF CONICAL SPOUTED BED FLUID DYNAMICS

Article Highlights

- A conical spouted bed, applied to drying operations, was simulated by CFD-DEM
- Different particle rotation conditions, turbulence, and drag models are evaluated
- Analysis of particle rotation indicates its importance in CFD-DEM simulation
- Koch-Hill and Gidaspow drag models showed better agreement with the experimental data
- The standard *k-ε* turbulence model showed a greater agreement with experimental data

Abstract

The input parameters, empirical, and semi-empirical models significantly influence the responses obtained by CFD-DEM simulations. In this work, the effects of three turbulence models, three conditions of the particle rotation, and five drag models, on the fluid dynamic behavior of a conical spout bed applied to the drying of sorghum grains were evaluated. Experimental data on the solids pressure drop, height, and shape of the fountain were used to validate the simulations. Results showed the importance of including the particle rotation in the model to approximate the results simulated with the experimental behavior. Compared with experimental data, considering the particle rotation by the Dennis et al. model, the deviation was 2% for the fountain height and 9.18% for the pressure drop. Whereas, for the model without the particle rotation, the deviations were 106.33 and 42.31% for the fountain height and pressure drop, respectively. For the analyzed case, the standard k-ε turbulence model showed a greater agreement with the experimental data. For the drag models evaluated, the best fit with the experimental data was obtained by the Koch-Hill drag model, followed by the Gidaspow model, with deviations less than 10%.

Keywords: drag model, particle rotation, turbulence model, sorghum grains.

The mathematical modeling of the fluid dynamic behavior in spouted beds follows two main methods. The first, known as two-fluid model (TFM), considers the solid and fluid phases as continuous and interpenetrating, and the properties of the solid phase can be described by the kinetic theory of granular flow (KTGF). This approach is widely used [1-4]. The second, called computational fluid dynamics/discrete element method coupled (CFD-DEM), considers the fluid phase as continuous, while the solid phase is treated as discrete from the modeling of the individual motion of each particle present in the system. Studies that employ CFD-DEM are being conducted mainly to evaluate fluid dynamics characteristics [5-8]. Through this method, it is possible to obtain information on the particle scale, such as the forces acting between particle-particle, particle-wall, as well as track the particle individually. For the success of simulations applying this approach, it is essential to determine the DEM input parameters, which are divided into: material properties (average equivalent diameter, sphericity and specific mass) and interaction

Correspondence: R. Béttega, Federal University of São Carlos, Department of Chemical Engineering, SP, Brazil.
E-mail: bettega@ufscar.br
Paper received: 15 September, 2020
Paper revised: 18 December, 2020
Paper accepted: 8 January, 2021

https://doi.org/10.2298/CICEQ110707002B

properties (restitution coefficient, static friction coefficient, and rolling friction coefficient).

In the CFD-DEM coupled, many parameters and models are applied to describe the behavior of the solid and fluid phases, and these have a great influence on the simulated response. Rotation is a natural feature of particle motion. Marchelli *et al.* [9] mention the importance of considering its effect, mainly in gas--solid flows involving particles with larger diameters. The authors analyzed the influence of the rotational drag force and the effect of neglecting the particle rotation on the dynamics of glass spheres in a pseudo-2D spouted bed. The simulated results showed that in neglecting the particle rotation, there was an imprecise prediction of the particle motion, though this consideration did not affect the formation of a central and linear spout channel, and oscillations could be observed. Although its effect is important, in many studies it is neglected.

Turbulence is an important point in CFD simulations and can have a strong influence on the simulated results. Turbulence models can be grouped into three classes: direct numerical simulation (DNS), large Eddy simulation (LES), and Reynolds-average Navier-Stokes (RANS). Within the RANS modeling, with regard to the two equation turbulence models, the standad k-ε model is widely used, due to its robustness, lower computational cost and reasonable precision for a wide range of turbulent flows. Proposed by Launder and Spalding [10], the k-ε model describes the freestream flow regions. The SST k-ω model includes both a model for addressing the wall regions and another for the regions with greater turbulence, interspersing the standard model k-ω and the model k-ε, respectively. This model was developed by Menter [11]. Regarding the use of turbulence models in CFD-DEM simulations applied to spouted beds, the most applied are: standard k-ε [5,12,13], RNG k-ε [14], realizable k-ε [15], and SST k-ω [16]. In some studies, turbulence is not considered in CFD--DEM simulations [17,18]. Marchelli *et al.* [9] investigated the effect of four turbulence models (standard k-ε model, standard k-ε model with an enhanced wall treatment (EWT), realizable k-ε model, standard k-ω model) and lack of a turbulence model (laminar case) in spouted bed by CFD-DEM simulations. The standard k-ε and k-ω models produce almost identical results. Accord to Yang *et al.* [19], an appropriate turbulence model is necessary to predict the central jet that penetrates the bed materials, since the lack of knowledge of the turbulence results in the difficulty to model the spout-annulus interface in the spouted bed. However, it should be noted that there is no consensus on the most appropriate model to describe the turbulence in spouted beds using CFD-DEM simulations.

The drag is mainly responsible for the momentum exchange between the phases in a gas-solid flow. The literature reports several models to obtain the drag coefficient. In TFM simulations, the Gidaspow drag model [20] is widely used in spouted bed simulations [3,4,21-23]. However, there is no such agreement for CFD-DEM simulations. The drag models most used in CFD-DEM simulations are: Wen and Yu [24], Gidaspow [20] and Di Felice [25], developed through classical approaches (*e.g.*, empirical methods), and models proposed by means of Lattice-Boltzmann simulations: Rong, Dong, Yu [26], Beetstra, Van Der Hoef, Kuipers [27], Koch and Hill [28]. In order to evaluate the effect of these models in CFD--DEM simulations, several studies have been developed to identify the influence of the drag model in the simulations. He *et al.* [29] evaluated the influence of Gidaspow [20], and Koch and Hill [28] drag models in a rectangular fluidized bed with dry and wet granular systems. The authors found better results simulated by the drag model by Koch and Hill [28]. Zhang *et al.* [30] analyzed the binary mixture segregation of glass spheres (2.5 and 1.5 mm) in a rectangular fluidized spouted bed evaluating different drag models [20,26,31,32]. The results predicted by Rong, Dong, Yu [26] presented smaller deviations (5.3%) compared to the experimental. Pietsch *et al.* [15] analyzed the particle dynamics of a three-dimensional prismatic spouted bed using the drag models of Beetstra, Van Der Hoef, Kuipers [27], Di Felice [25], Gidaspow [20], and Koch and Hill [28]. The drag models of Beetstra, Van Der Hoef, Kuipers [27] and Koch and Hill [28] predicted with greater precision the expansion of the bed and the establishment of the spout regime. Furthermore, Marchelli *et al.* [13] employed the four drag models described above, added to the Rong, Dong, Yu [26], Tenneti, Garg, Subramaniam [33] and Wen and Yu [24] to evaluate the fluid dynamics of two spouted beds in different configurations (pseudo-2D and 3D cylindrical). The authors observed that in the simulations where the minimum fluidization flow was applied, only the Gidaspow model [20] can predict the fluidization, but for low air flow rates, the Beetstra, Van Der Hoef, Kuipers [27] model was more suitable for predicting the characteristic behavior of the spouted bed.

The simulated results vary significantly with the models used to calculate the drag force, turbulence, and particle rotation, among others. In many cases, models are used without justification. Generally, the

simulated data is not validated with experimental data, only a qualitative analysis is performed. Thus, due to lack of agreement on which drag model is more effective for the experimental data reproducibility, we assessed the influence of drag models of Beetstra, Van Der Hoef, Kuipers [27], Di Felice [25], Gidaspow [20], Koch and Hill [28] and Rong, Dong, Yu [26]. In addition to the drag models, the effect of standard k-ε, realizable k-ε, and SST k-ω turbulence models were also analyzed, and the influence of the particle rotation condition, considering the torque equal to zero, calculating the rotational drag coefficient by the model of Dennis *et al.* [34], and neglecting the particle rotation, on the fluid dynamic behavior of the conical spouted bed applied to drying operations, operating with sorghum grains through CFD--DEM simulations. Experiments were carried out to validate the models analyzed.

EXPERIMENTAL METHODOLOGY

Experimental unit

The spouted bed used in the experiments was constructed in acrylic, with a cylindrical column with a height of 30 cm and a diameter of 14.2 cm, with a 60° conical base with a height of 11 cm and a lower diameter of 2.5 cm. A Venturi-type air distributor was attached to the bottom of the conical base. Figure 1a shows the dimensions of the equipment.

Experimental procedure

Fluid dynamic tests were performed according to the methodology proposed by Mathur and Epstein [35]. The tests were carried out in triplicate, for 500 g of sorghum grains. This method consists of obtaining pressure drop curves as a function of air velocity for increasing velocities (fixed bed to stable spout regime) and decreasing velocities (stable spout regime to fixed bed).

Sorghum grains characterization

In this work, sorghum grains were used as particulate material. The characterization of this material was carried out in a previous work [5]. Therefore, the physical and particle-particle interaction properties were the same as in this work. To obtain the particle-wall interactions, the methodology described in this work was used, using an acrylic surface with the same characteristics as the spouted bed wall (thickness of 3 mm).

MATHEMATICAL METHODOLOGY

Mathematical modeling

Simulations were performed using the CFD--DEM coupled. The fluid phase was assumed to be continuous, with its motion described by the Navier-Stokes equations, since air is considered a Newtonian fluid. The particulate phase was treated as a discrete phase and the particle motion was evaluated using Newton's second law.

Equations of governing fluid phase

The mass and momentum conservation equations for the fluid phase are presented in Eqs. (1) and (2), respectively:

$$\frac{\partial}{\partial t}\left(\alpha_f \rho_f\right) + \nabla \cdot \left(\alpha_f \rho_f \vec{v}_f\right) = 0 \quad (1)$$

$$\frac{\partial}{\partial t}\left(\alpha_f \rho_f \vec{v}_f\right) + \nabla \cdot \left(\alpha_f \rho_f \vec{v}_f \vec{v}_f\right) = \alpha_f \nabla p + \nabla . \bar{\bar{\tau}}_f - \vec{F} + \alpha_f \rho_f \vec{g} \quad (2)$$

where α_f, ρ_f, $\vec{v}_f$, ∇p, and $\bar{\bar{\tau}}_f$ are the volume fraction, density, velocity, pressure, and shear stress of the

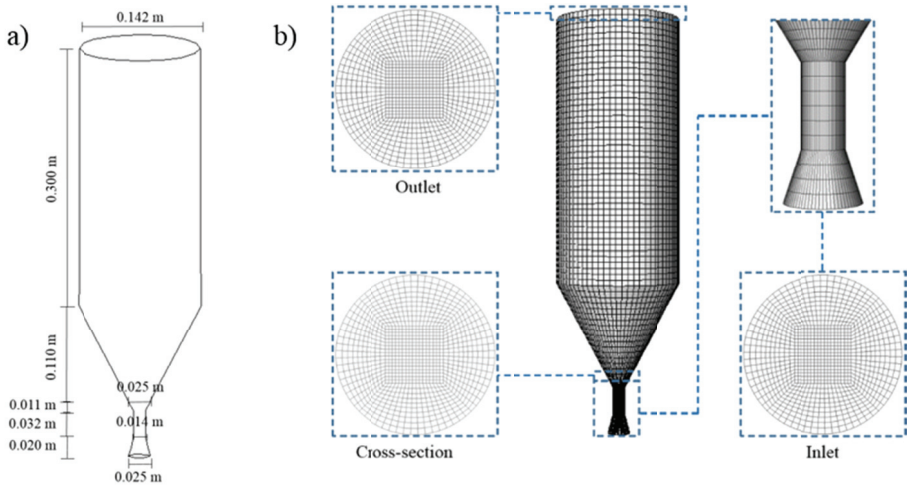

Figure 1. a) schematic illustration of the spouted bed; b) representation of the computational grid.

fluid phase, respectively, and $\vec{g}$ is the gravitational acceleration.

The fluid volume fraction (α_f) in a computational cell (V_{cel}) can be estimated by Eq. (3) [36]:

$$\alpha_f = 1 - \frac{1}{V_{cel}} \sum_{i=1}^{k_v} \sigma_i V_{s,i} \quad (3)$$

where σ_i is the volume fraction of particle *i* in the fluid cell.

Drag force. The volumetric fluid-particle interaction force ($\vec{F}$) can be obtained using the drag force, according to Eq. (4):

$$\vec{F} = \frac{1}{V_{cel}} \sum_{i=1}^{k_v} \vec{f}_i^{\,d} \quad (4)$$

where V_{cel} is the volume of the computational cell and k_v is the number of particles in the cell.

The drag force ($\vec{f}_i^{\,d}$) can be calculated using Eq. (5):

$$\vec{f}_i^{\,d} = \frac{V_{s,i}\beta_{fs}}{1-\alpha_f}\left(\vec{v}_f - \vec{v}_s\right) \quad (5)$$

where $V_{s,i}$ and $\vec{v}_s$ are the volume and velocity of the particle, respectively. β_{fs} is the interphase momentum exchange coefficient, obtained by:

$$\beta_{fs} = \frac{\alpha_s \mu_f}{d_s^2} D \quad (6)$$

where α_s and d_s are the volume fraction and diameter of the particles, respectively, μ_f is the fluid viscosity. D is the drag function; it can be calculated with different drag models. Most of these models are of empirical or half-empirical nature. In this study, different drag models were investigated.

Gidaspow drag model

Through the Gidaspow model [20], D is calculated by:

$$D = 18\alpha_f{}^{-3.65}\left[1 + 0.15\left(\alpha_f Re_s\right)^{0.687}\right], \quad \alpha_f > 0.8 \quad (7)$$

$$D = 150\frac{\alpha_s}{\alpha_f{}^2} + 1.75\frac{Re_s}{\alpha_f}, \quad \alpha_f \le 0.8 \quad (8)$$

$$Re_s = \frac{\rho_f d_s |\vec{v}_s - \vec{v}_f|}{\mu_f} \quad (9)$$

Di Felice drag model

For the Di Felice model [25], D is obtained as:

$$D = 0.75 C_D Re_s \alpha_f{}^{2-\chi} \quad (10)$$

$$C_D = \left(0.63 + \frac{4.8}{\sqrt{\alpha_f Re_s}}\right)^2 \quad (11)$$

$$\chi_{Di\ Felice} = 3.7 - 0.65 e^{\left\{-\frac{\left[1.5 - log_{10}\left(\alpha_f Re_s\right)\right]^2}{2}\right\}} \quad (12)$$

where C_D is the drag force coefficient, and Re_s is the particle Reynolds number.

Rong, Dong, Yu drag model

The Rong, Dong, Yu [26] model can be considered an enhancement of the Di Felice drag model [25]; it uses the same drag function, and only varies in the definition of χ:

$$\chi_{Rong} = 2.65\left(\alpha_f + 1\right) - (5.3 - 3.5\alpha_f)\alpha_f^2 e^{\left\{-\frac{\left[1.5 - log_{10}\left(\alpha_f Re_s\right)\right]^2}{2}\right\}} \quad (13)$$

Koch and Hill drag model

In the Koch and Hill model [28], the drag function (D) is calculated by:

$$D = 18\alpha_f(F_0 + 0.5F_1\alpha_f Re_s) \quad (14)$$

$$F_0 = \frac{1+3\sqrt{\frac{\alpha_s}{2}}+\frac{135}{64}\alpha_s \ln(\alpha_s)+16.14\alpha_s}{1+0.681\alpha_s-8.48\alpha_s^2+8.16\alpha_s^3}, \quad \alpha_s \le 0.4 \quad (15)$$

$$F_0 = \frac{10\alpha_s}{\alpha_s^3}, \quad \alpha_s > 0.4 \quad (16)$$

$$F_1 = 0.0673 + 0.212\alpha_s + 0.0232\alpha_f^{-5} \quad (17)$$

Beetstra, Van Der Hoef, Kuipers drag model

For the Beetstra, Van Der Hoef, Kuipers model [27], the drag function (D) is obtained by the equation:

$$D = 18\alpha_f F_B \quad (18)$$

$$F_B = 10\frac{\alpha_s}{\alpha_s^2} + \alpha_s^2\left(1 + 1.5\sqrt{\alpha_s}\right) + \frac{\left(\frac{0.413 Re_s}{24\alpha_s^2}\right)\left(\frac{1}{\alpha_s}+3\alpha_f\alpha_s+8.4Re_s^{-0.343}\right)}{1+10^{3\alpha_s}Re_s^{-0.5-2\alpha_s}} \quad (19)$$

Turbulence. The Reynolds stress tensor of the fluid phase ($\bar{\bar{\tau}}_f$) is expressed as follows:

$$\bar{\bar{\tau}}_f = -\frac{2}{3}\left(\alpha_f\rho_f k + \alpha_f\rho_f\mu_{f,t}\nabla\cdot\vec{v}_f\right)\bar{\bar{I}} + \alpha_f\rho_f\mu_{f,t}\left(\nabla\vec{v}_f + \nabla\vec{v}_f^{\,T}\right) \quad (20)$$

For modeling the turbulence, two-equation models are historically the most widely used turbulence models in industrial CFD. Examples of such models are the *k-ε* and *k-ω* models in their different forms. They solve two transport equations and model the Reynolds stresses using the turbulent viscosity approach.

Standard k-ε model

The standard *k-ε* model for the dispersed phase was used to simulate the turbulent nature of the bed flow. The turbulent viscosity ($\mu_{f,t}$) is computed as:

$$\mu_{f,t} = \rho_f C_\mu \frac{k^2}{\varepsilon} \quad (21)$$

where C_μ is a constant that was set to 0.09 in all simulations. The parameters k and ε are the turbulence kinetic energy and turbulence energy dissipation

rate, respectively, which are governed by the following transport equations:

$$\frac{\partial}{\partial t}\left(\alpha_f \rho_f k\right) + \nabla \cdot \left(\alpha_f \rho_f \vec{v}_f k\right) = \nabla \cdot \left(\alpha_f \frac{\mu_{t,f}}{\sigma_k} \nabla k\right) + \alpha_f G_k - \alpha_f \rho_f \varepsilon \quad (22)$$

$$\frac{\partial}{\partial t}\left(\alpha_f \rho_f \varepsilon\right) + \nabla \cdot \left(\alpha_f \rho_f \vec{v}_f \varepsilon\right) = \nabla \cdot \left(\alpha_f \frac{\mu_{t,f}}{\sigma_\varepsilon} \nabla \varepsilon\right) + \alpha_f \frac{\varepsilon}{k}\left(C_1 G_k - C_2 \rho_f \varepsilon\right) \quad (23)$$

where σ_k=1 and σ_ε=1.3 are the turbulent Prandtl numbers for k and ε, respectively. C_1=1.44 and C_2=1.92 are model constants. G_k denotes the generation of turbulence kinetic energy by the mean velocity gradient and is given by:

$$G_k = \mu_{f,t}\left(\nabla \vec{v}_f + \left(\nabla \vec{v}_f\right)^{\mathrm{T}}\right) : \nabla \vec{v}_f \quad (24)$$

Realizable k-ε model

The turbulent viscosity ($\mu_{f,t}$) is calculated in the same form as the standard k-ε model. But, in the realizable k-ε model, C_μ is not constant. It is computed from:

$$C_\mu = \frac{1}{4.04 + A_s \frac{kU^*}{\varepsilon}} \quad (25)$$

$$U^* \equiv \sqrt{S_{ij} S_{ij} + \widetilde{\Omega}_{ij} \Omega_{ij}} \quad (26)$$

$$\widetilde{\Omega}_{ij} = \Omega_{ij} - 2\varepsilon_{ijk}\omega_k \quad (27)$$

$$\Omega_{ij} = \overline{\Omega_{ij}} - \varepsilon_{ijk}\omega_k \quad (28)$$

where $\overline{\Omega_{ij}}$ is the mean rate-of-rotation tensor viewed in a moving reference frame with the angular velocity ω_k. The constant A_s is given by:

$$\mathrm{A}_s = \sqrt{6} cos\varphi \quad (29)$$

$$\varphi = \frac{1}{3} cos^{-1}\left(\sqrt{6} W\right) \quad (30)$$

$$W = \frac{S_{ij} S_{jk} S_{ki}}{\tilde{S}^3} \quad (31)$$

$$\tilde{S}^3 = \sqrt{S_{ij} S_{ij}} \quad (32)$$

$$S_{ij} = \frac{1}{2}\left(\nabla \vec{v}_f\right) \quad (33)$$

The modeled transport equations for k and ε in the k-ε realizable model are:

$$\frac{\partial}{\partial t}\left(\alpha_f \rho_f k\right) + \nabla \cdot \left(\alpha_f \rho_f \vec{v}_f k\right) = \nabla \cdot \left(\alpha_f \frac{\mu_{t,f}}{\sigma_k} \nabla k\right) + \alpha_f G_k - \alpha_f \rho_f \varepsilon \quad (34)$$

$$\frac{\partial}{\partial t}\left(\alpha_f \rho_f \varepsilon\right) + \nabla \cdot \left(\alpha_f \rho_f \vec{v}_f \varepsilon\right) = \nabla \cdot \left(\alpha_f \frac{\mu_{t,f}}{\sigma_\varepsilon} \nabla \varepsilon\right) + \alpha_f \varepsilon C_1 S - \alpha_f C_2 \rho_f \frac{\varepsilon^2}{k + \sqrt{\nu\varepsilon}} \quad (35)$$

$$C_1 = max\left[0.43, \frac{\eta}{\eta + 5}\right] \quad (36)$$

$$\eta = S\frac{k}{\varepsilon} \quad (37)$$

$$S = \sqrt{2 S_{ij} S_{ij}} \quad (38)$$

where σ_ε=1.2.

SST k-ω model

For the SST k-ω model, the turbulent viscosity ($\mu_{f,t}$) is computed as:

$$\mu_{f,t} = \frac{\rho_f k}{\omega} \frac{1}{max\left[\frac{1}{\alpha^*}, \frac{SF_1}{\alpha_1 \omega}\right]} \quad (39)$$

$$F_1 = tanh(\phi_1^2) \quad (40)$$

$$\phi_1 = max\left[2\frac{\sqrt{k}}{0.09\omega y}, \frac{500\mu_f}{\rho_f y^2 \omega}\right] \quad (41)$$

where S is the strain rate magnitude, and where y is the distance to the next surface.

The turbulence kinetic energy, k, and the specific dissipation rate, ω, are obtained from the following transport equations:

$$\frac{\partial}{\partial t}\left(\alpha_f \rho_f k\right) + \nabla \cdot \left(\alpha_f \rho_f \vec{v}_f k\right) = \nabla \cdot \left[\alpha_f \left(\mu_f + \frac{\mu_{f,t}}{\frac{1}{\frac{F_2}{\sigma_{k,1}} + \frac{1 - F_2}{\sigma_{k,2}}}}\right) \nabla k\right] + \alpha_f G_k \quad (42)$$

$$\frac{\partial}{\partial t}\left(\alpha_f \rho_f \omega\right) + \nabla \cdot \left(\alpha_f \rho_f \vec{v}_f \omega\right) = \nabla \cdot \left[\alpha_f \left(\mu_f + \frac{\mu_{t,f}}{\frac{1}{\frac{F_2}{\sigma_{\omega,1}} + \frac{1 - F_2}{\sigma_{\omega,2}}}}\right) \nabla \omega\right] + \alpha_f G_\omega \quad (43)$$

where:

$$F_2 = tanh(\phi_2^4) \quad (44)$$

$$\phi_2 = min\left[max\left(\frac{\sqrt{k}}{0.09\omega y}, \frac{500\mu_f}{\rho_f y^2 \omega}, \frac{4\rho_f k}{\sigma_{\omega,2} D_\omega^+ y^2}\right)\right] \quad (45)$$

$$D_\omega^+ = max\left(2\rho_f \frac{1}{\sigma_{\omega,2}} \frac{1}{\omega} \nabla k \nabla \omega, 10^{-10}\right) \quad (46)$$

$\sigma_{k,1}$=1.176, $\sigma_{\omega,1}$=2.0, $\sigma_{k,2}$=1.0, $\sigma_{\omega,2}$=1.168 and α_1=0.32 are model constants. G_ω represents the generation of ω and is given by:

$$G_\omega = \frac{\rho_f \alpha \alpha^*}{\mu_{f,t}} G_k \quad (47)$$

where:

$$\alpha^* = \alpha_\infty \left(\frac{0.24 + \frac{\rho_f k}{6\mu_f \omega}}{1 + \frac{\rho_f k}{6\mu_f \omega}}\right) \quad (48)$$

$$\alpha_\infty = 0.55 F_2 + 0.44(1 - F_2) \quad (49)$$

More details about the turbulence models can be seen in [37].

Equations of particle motion

A particle with mass m_i and moment of inertia I_i has translational and rotational motions, described by Eqs. (50) and (51), respectively:

$$m_i \frac{d\vec{v}_{si}}{dt} = \vec{f}_i^{\,d} + \vec{f}_{ij}^{\,c} + \vec{f}_i^{\,g} \tag{50}$$

$$I_i \frac{d\vec{\omega}_i}{dt} = \vec{T} = \frac{\rho_f}{2}\left(\frac{d_p}{2}\right)^5 C_\omega |\vec{\Omega}|.\vec{\Omega} \tag{51}$$

where $\vec{v}_{si}$ and $\vec{\omega}_i$ are the translational and angular velocities of particle *i*, respectively, $\vec{f}_i^{\,g}$ is the gravitational force, $\vec{f}_{ij}^{\,c}$ is the contact force acting on particle *i* by particle *j* or the wall, $\vec{T}$ is the torque, C_ω is the rotational drag coefficient, and $\vec{\Omega}$ is the relative particle-fluid angular velocity.

Rotation is a natural characteristic of particle motion. To evaluate the effect of the particle rotation in the fluid dynamics of the spouted bed, simulations were performed neglecting the particle rotation (where Eq. (51) is neglected), considering the torque equal to zero ($\vec{T} = 0$), and calculating the rotational drag coefficient by Eq. (52), developed by Dennis *et al.* [34]:

$$C_\omega = \frac{6{,}45}{\sqrt{Re_\omega}} + \frac{32{,}1}{Re_\omega} \tag{52}$$

$$Re_\omega = \frac{\rho_f |\vec{\Omega}| d_s^2}{4\mu_f} \tag{53}$$

where Re_ω is the rotational Reynolds number.

In the soft-sphere approach, the particles slightly overlap during collisions, considering the unit vector $\vec{e}_{12}$ and the overlap (δ) of two colliding particles 1 and 2, defined by Eqs. (54) and (55), respectively:

$$\vec{e}_{12} = \frac{(\vec{x}_2 - \vec{x}_1)}{\|\vec{x}_2 - \vec{x}_1\|} \tag{54}$$

where $\vec{x}_1$ and $\vec{x}_2$ represent the particle position vectors 1 and 2, respectively.

$$\delta = \|\vec{x}_2 - \vec{x}_1\| - (r_1 - r_2) \tag{55}$$

where r_1 and r_2 represent the radii of particles 1 and 2, respectively.

The spring-dashpot collision law requires the definition of a spring constant (K), as in the spring collision law, along with a coefficient of restitution (η) for the dashpot term:

$$\vec{F}_1 = -\vec{F}_2 = (K\delta + \gamma(\vec{v}_{12}.\vec{e}_{12}))\vec{e}_{12} \tag{56}$$

in which:

$$f_{loss} = \sqrt{\pi^2 + ln^2\eta} \tag{57}$$

$$m_{12} = \frac{m_1 m_2}{m_1 + m_2} \tag{58}$$

$$t_{coll} = f_{loss}\sqrt{\frac{m_{12}}{K}} \tag{59}$$

$$\gamma = -2\frac{m_{12} ln\eta}{t_{coll}} \tag{60}$$

$$\vec{v}_{12} = \vec{v}_2 - \vec{v}_1 \tag{61}$$

where f_{loss} is a loss factor, m_1 and m_2 are the masses of particles 1 and 2, respectively, m_{12} is the so-called "reduced mass", t_{coll} is the collision time scale, $\vec{v}_1$ and $\vec{v}_2$ are the velocities of particles 1 and 2, respectively, $\vec{v}_{12}$ is the relative velocity, and γ is the damping coefficient.

The friction force between the particles was based on the Coulomb friction law:

$$\vec{F}_{friction} = (\mu_s + \mu_R)\vec{F}_{normal} \tag{62}$$

where μ_s is the static friction coefficient, μ_R is the rolling friction coefficient, and $\vec{F}_{normal}$ is the magnitude of the force normal to the surface.

Simulation setup and computational grid

To evaluate the models, CFD-DEM simulations were performed for the air inlet velocity of 22 m/s and a mass of 500 g of sorghum grains, which corresponds to 21,300 particles. The simulations were performed using the Fluent® software. The geometries were constructed in Design Modeler and the grids were generated using Meshing, which is available in Ansys® Student version 19.1. The 3D computational grid was constructed in accordance with the spacing between nodes determined in the grid independence test performed in our previous work [5]. The computational grid showed spacing between the nodes of $1d_s$ in the Venturi air distributor. On the conical base, the spacing between nodes was $1.35d_s$ at the entrance of the cone, and $8d_s$ at the intersection with the cylinder, and $8d_s$ in the cylindrical region, totaling 1.680 cells. Figure 1b shows the computational grid used in the CFD-DEM simulations.

The particle-particle and particle-wall interaction properties employed in the CFD-DEM simulations are shown in Table 1.

Table 1. Interaction properties

Interaction	η	μ_S	μ_R
Particle-particle	0.46±0.02	0.79±0.09	0.70±0.10
Particle-wall	0.53±0.04	0.65±0.05	0.33±0.06

Table 2 shows the models and parameters of the numerical solution used in the CFD-DEM simulations.

In CFD-DEM simulations, some considerations were made. The modeling assumes an isothermal

condition, with the physical properties of the solid phase constant ($\rho_s = 1300\,\frac{kg}{m^3}, d_s = 0{,}0032\,m, \varphi = 1$), and the air properties were also constant.

Table 2. Boundary conditions, models and numerical solution parameters adopted in CFD-DEM simulations

Boundary conditions	Inlet: inlet velocity
	Outlet: outlet pressure
	Wall: no-slip for the fluid phase
Solution methods	Pressure-velocity coupling was obtained using the SIMPLE algorithm
	Spatial discretization:
	Momentum: QUICK
	Volume fraction: QUICK
	Turbulence: First order upwind
	Transient formulation: First order implicit
Turbulence	Turbulent intensity: 5%
	Turbulent viscosity ratio: 10
Spring constant (*K*)	1000 N/m
Convergence criterion	$1x10^{-3}$
Time step	Fluid phase: $1x10^{-4}$
	Solid phase: $2x10^{-5}$
Time step number	100,000
Max. iterations/time step	200
Under-relaxation factors	Momentum: 0.2
	Volume fraction: 0.5
	Discrete phase: 0.5

Drag models from Beetstra, Van Der Hoef, Kuipers [27], Di Felice [25], Koch and Hill [28] and Rong, Dong, Yu [26] were implemented to Fluent® through UDF (user defined function). The Gidaspow model [20] is available on Fluent®.

RESULTS AND DISCUSSION

Fluid dynamics analysis

Figure 2 shows the fluid dynamics curves obtained experimentally for the 500 g of sorghum grains; the results show a satisfactory reproducibility between the curves. Through a qualitative analysis, the typical spouted bed behavior is observed. For low air velocities, the fluid just percolates through the bed, without particle motion, as shown in Figure 3i. With the increase in air velocity, the pressure drop also increases, reaching a maximum value with the formation of the internal jet and an increase in the arc of solids (Figure 3ii). Then, with an additional increase in air velocity, the internal jet becomes extended in relation to the compact arc of solids, reducing the pressure drop, and the downward motion of the solids in the annular region begins. Subsequently, the solids are dragged into the central region, the bed expands, further reducing the pressure drop. With an increase in air velocity, the incipient spout is observed and then the minimum spout condition is observed (Figure 3iii). After the minimum spout condition, the spout becomes stable. The minimum spouting velocity is an important operational parameter, the value measured for the mass of 500 g was 17.10±0.20 m/s.

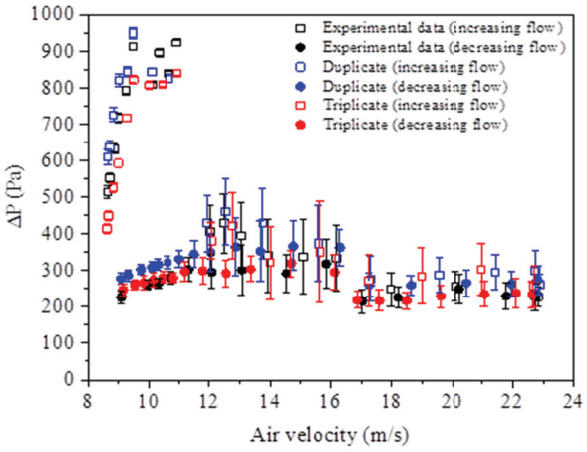

Figure 2. Experimental fluid dynamic curves for the 500 g mass.

After carrying out the experiments, simulations were conducted at an air velocity of 22 m/s, corresponding to the stable spout regime.

Effect of particle rotation

The results were obtained considering an average of 6 s of simulated real time. Figure 4 shows the experimental flow pattern, simulated by CFD-DEM using the Dennis *et al.* [34] model to calculate the rotational drag coefficient (Eq. (52)), considering the torque equal to zero, and neglecting the particle rotation. Similar behavior can be seen when the Dennis *et al.* [34] model was used to calculate the rotational drag coefficient and considering the torque equal to zero; the behavior was similar to the experimental behavior. When the particle rotation was neglected, a flow pattern different from the experimental can be observed, with a high and diluted fountain.

To quantify these observations, it was based on fountain height and pressure drop, parameters characteristic of the spouted bed. Table 3 presents the simulated results for the different conditions of particle rotation and experimental results for the fountain height and pressure drop.

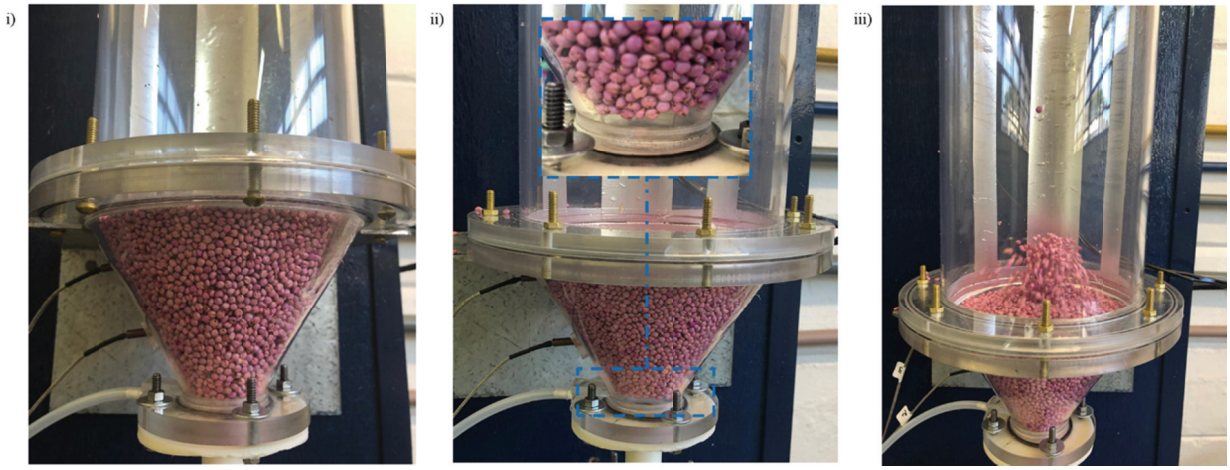

Figure 3. Development of a spouted regime: i) fixed bed; ii) internal jet (arc of solids); iii) minimum spout.

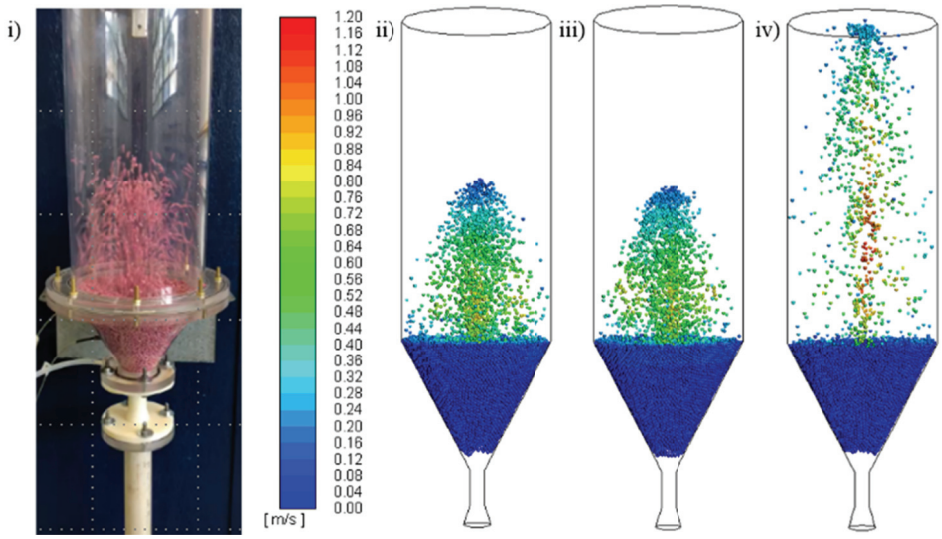

Figure 4. Solids flow pattern: i) experimental; ii) Dennis et al. [34] model; iii) $\vec{T} = 0$; iv) without particle rotation.

Table 3. Comparison between experimental data of fountain height and pressure drop, and simulated by different rotation conditions

Condition	H_f (m)	Deviation (%)	ΔP (Pa)	Deviation (%)
Experimental	14.54		238.27	
Dennis *et al.* [34]	14.83	-2.00	216.40	9.18
$\vec{T} = 0$	13.80	5.08	206.90	13.16
Without particle rotation	30	106.33	137.45	42.31

For both parameters, the deviations between the experimental data and data simulated by the Dennis *et al.* [34] model were lower than 10%. Although the case in which the torque was equal to zero showed a low deviation from the experimental value, this hypothesis is less realistic, since the angular velocity is assumed constant. The highest deviation observed when neglecting the particle rotation is coherent, since the particle rotation is a phenomenon observed experimentally. The deviations between experimental and simulated data can be related to some simplification by the model used, as the angular velocity calculation. For the simulations to evaluate the turbulence models, the Dennis *et al.* [34] model was chosen, because this model had better agreement with the experimental data.

Effect of the turbulence models

There are several turbulence models reported in the literature. The *k-ω* model is known to provide better results in the wall regions. However, for the spouted bed simulated in this work, it can be seen in Figure 5a that results for the standard *k-ε* and SST *k-ω* models are similar in the region close to the wall. This result may be related to the fact that the computational grid employed in CFD-DEM simulations shows

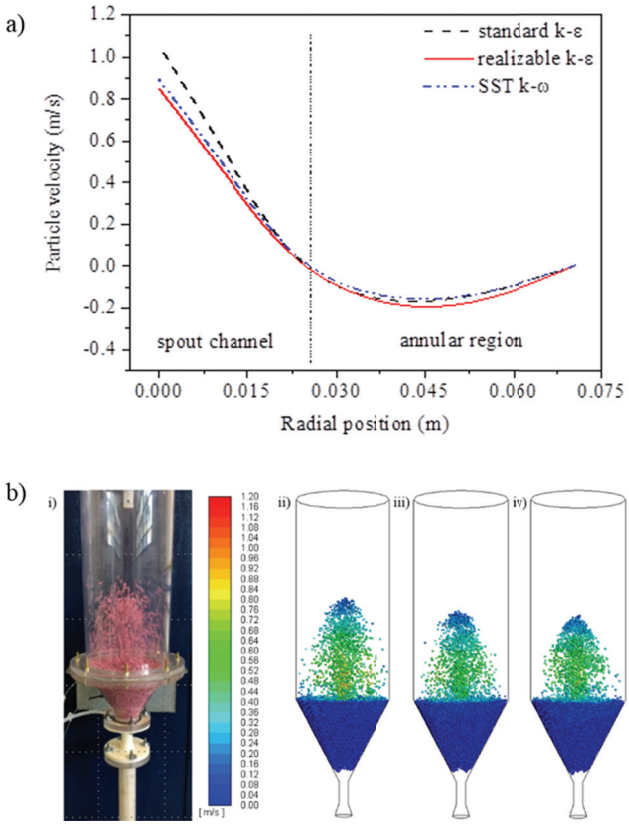

Figure 5. a) particle velocity for different turbulence models at the position of 0.173 m; b) solids flow pattern for different turbulence models: i) experimental; ii) standard k-ε; iii) realizable k-ε; iv) SST k-ω.

high spacing between nodes, which may have minimized the effects of the SST *k-ω* model in the wall region; a similar observation was found in [9]. Figure 5b shows the fountain shape obtained experimentally, simulated by CFD-DEM using the standard turbulence *k-ε*, realizable *k-ε* and SST *k-ω* models. Table 4 shows the fountain height and pressure drop, experimental and simulated, for different turbulence models. Qualitatively, these parameters showed that the best fit was obtained for the standard *k-ε* model. Thus, for the conditions simulated in this work, the standard *k-ε* model was the most adequate.

Table 4. Comparison between experimental data of fountain height and pressure drop, and data simulated by the different turbulence models

Model	H_f (m)	Deviation (%)	ΔP (Pa)	Deviation (%)
Experimental	14.54		238.27	
Standard *k-ε*	14.83	-2.00	216.40	9.18
Realizable *k-ε*	13.26	8.80	209.70	11.99
SST *k-ω*	12.56	13.62	207.46	12.93

CFD-DEM simulations carried out with the objective of evaluating the drag models were performed using the standard *k-ε*, and the Dennis *et al.* [34] model, since these models showed better agreement with the experimental data.

Effect of the drag models

Figure 6a shows the experimental flow pattern obtained by the different drag models for the inlet air velocity of 22 m/s. It can be observed that there was no particle drag for the models of Di Felice [25], and Rong, Dong, Yu [26]; the bed of solids remained static for both models. According to Marchelli *et al.* [13], Di Felice [25] and Rong, Dong, Yu [26] models produce similar values for the drag force. Greater fountain heights and a very similar behavior between the models of Gidaspow [20], and Koch and Hill [28] can be verified, which are in accordance with the experimental flow pattern. Although the equations for calculating the drag coefficient are different, the two models present different equations for the different fluid volumetric fraction ranges (porosity). The Beetstra, Van Der Hoef, Kuipers [27] model underestimated the solid drag, with a small and narrow fountain.

To quantify the simulated results, Table 5 presents a comparison between the fountain height and pressure drop data, experimental and simulated, with the different drag models. Both for the fountain height

and for the pressure drop, it can be verified that the Gidaspow [20], and Koch and Hill [28] models presented low deviations in relation to the experimental value. As for the pressure drop, there is a smaller deviation for the Beetstra, Van Der Hoef, Kuipers [27] model, however, this model showed a high deviation for the fountain height. High deviations were observed for Di Felice [25], and Rong, Dong, Yu [26] models for both evaluated properties.

Table 5. Comparison between experimental data of fountain height and pressure drop, and data simulated by different drag models

Model	H_f (m)	Deviation (%)	ΔP (Pa)	Deviation (%)
Experimental	14.54		238.27	
Beetstra [21]	9.43	35.14	236.24	0.85
Di Felice [19]	0	100.00	368.94	54.84
Gidaspow [12]	14.83	-2.00	216.40	9.18
Koch and Hill [22]	14.55	0.07	224.46	5.80
Rong [20]	0	100.00	354.04	48.59

Figure 6b shows the axial solid velocity as a function of the radial position for the five drag models analyzed. The data were obtained at the position of 0.173 m (referring to the static bed height, positioned at the intersection between the cone and the cylinder). It can be seen that the solids reach higher velocities in the spout channel for the models of Gidaspow [20], Koch and Hill [28], and Beetstra, Van Der Hoef, Kuipers [27] models, respectively, causing the larger fountain heights. This behavior is related to the higher drag force values obtained by these models. In spouted beds, drag is predominant in the spout channel, justifying the observed profiles. Zero velocity was observed for the models of Di Felice [25], and Rong, Dong, Yu [26].

CONCLUSIONS

The simulations showed the influence of the turbulence, drag, and particle rotation models on the results obtained, highlighting the importance of the appropriate choice of models for agreement with the experimental data. For the evaluated properties (solid flow pattern, fountain height, and pressure drop), the results obtained through the drag model of Koch and Hill [28], followed by the Gidaspow [20], were those that presented the best agreement with experimental data; deviations lower than 10% were obtained for these models. For the drag models of Di Felice [25], and Rong, Dong, Yu [26] there was no particle drag. For the case presented in this study, the standard k-ε turbulence model and the Dennis *et al.* [34] model were the most appropriate for calculating the rotational drag coefficient. The importance of considering

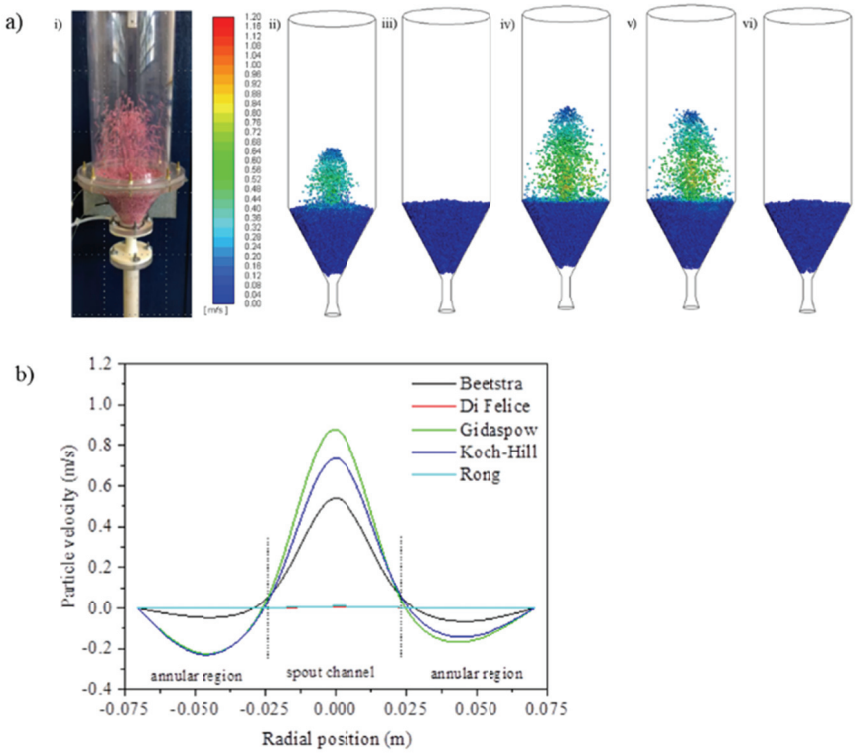

Figure 6. a) solids flow pattern for different drag models: i) experimental; ii) Beetstra, Van Der Hoef, Kuipers [21]; iii) Di Felice [19]; iv) Gidaspow [12]; v) Koch and Hill [22]; vi) Rong, Dong, Yu [20]; b) axial solid velocity for different drag models.

particle rotation to obtain a realistic behavior was also observed.

Acknowledgement

Authors appreciate the financial support from Coordenação de Aperfeiçoamento de Pessoal de Nível Superior - Brasil (CAPES) - Finance Code 001 and Conselho Nacional de Desenvolvimento Científico e Tecnológico - Brasil (CNPq).

Nomenclature

C_1, C_2, C_μ	Coefficients in turbulence model
C_D	Drag force coefficient
C_ω	Rotational drag coefficient
D	Drag function
d_s	Particle diameter, m
$\vec{f}_i^d$	Drag force on particle *i*, N
$\vec{f}_i^g$	Gravitational force on particle *i*, N
$\vec{f}_{ij}^c$	Contact force between particles *i* and *j*, N
$\vec{F}$	Volumetric force acting on particles by the surrounding fluid, N/m^3
G_k	Production of turbulent kinetic energy, J/(m^3·s)
$\vec{g}$	Gravitational acceleration, m/s^2
H_f	Fountain height, m
h_0	Static bed height, m
$\bar{\bar{I}}$	Unit tensor
I_i	Moment of inertia of particle *i*, kg/m^2
K	Spring stiffness, N/m
k_v	Number of particles in the cell
m_i	Mass of particle *i*, kg
p	Pressure, N/m^2
Re_s	Particle Reynolds number
Re_ω	Rotational Reynolds number
$\vec{T}$	Torque, N·m
t	Time, s
t_{coll}	Collision time, s
$\vec{v}$	Velocity, m/s
V	Volume, m³
V_{cell}	Volume of computational cell, m^3
$V_{s,i}$	Volume of particle *i*, m^3

Greek symbols

α	Volume fraction
β	Interphase momentum exchange coefficient
γ	Damping coefficient, kg/s
ε	Turbulence energy dissipation rate, m^2/s^3
ΔP	Pressure drop, Pa
δ	Overlap, m
η	Restitution coefficient
k	Turbulence kinetic energy, m^2/s^2
μ_f	Fluid viscosity, Pa·s
μ_s	Static friction coefficient
μ_R	Rolling friction coefficient
ρ	Density, kg/m^3
σ_i	Fraction of volume of particle *i* that is in the fluid cell
$\vec{\tau}_f$	Shear stress of fluid, N/m^2
φ	Sphericity
χ	Function of α_f and Re_s in the Di Felice and Rong models
Ψ	Asymptotic range
$\vec{\omega}_i$	Rotational velocity of particle *i*, rad/s
ω	Specific dissipation rate, m^2/s^3

Subscripts

f	Fluid
i	Particle *i*
j	Particle *j*
s	Solid/particle
w	Wall

Abbreviations

CFD	Computational fluid dynamics
DEM	Discrete element method
2D	Bidimensional
UDF	User defined function

REFERENCES

[1] B. Hooshdaran, S.H. Hosseini, M. Haghshenasfard, M.N. Esfahany, M. Olazar, CAppl. Therm. Eng. 127 (2017) 224-232

[2] E.F. Ahmadabadi, M. Haghshenasfard, M.N. Esfahany, Chem. Eng. Res. Des. 160 (2020) 476-485

[3] J.N.M. Batista, R.C. Brito, R. Béttega, Chem. Ind. Chem. Eng. Q. 24 (2018) 369-378

[4] A.S. Souza, J.T. Freire, R. Béttega, Ind. Eng. Chem. Res. 57 (2018) 13876-13888

[5] J.N.M. Batista, D.A. Santos, R. Béttega, Particuology (2020)

[6] F. Marchelli, D. Bove, C. Moliner, B. Bosio, E. Arato, Powder Technol. 321 (2017) 119-131

[7] H. Zhang, M. Liu, T. Li, Z. Huang, X. Sun, H. Bo, Y. Dong, Powder Technol. 307 (2017) 175-183

[8] S. Golshan, R. Zarghami, N. Mostoufi, Chem. Eng. Res. Des. 121 (2017) 315-328

[9] F. Marchelli, C. Moliner, B. Bosio, E. Arato, Powder Technol. 353 (2019) 409-425

[10] B. Launder, D.B. Spalding, Lectures in mathematical models of turbulence, Academic Press Inc, London, 1972

[11] F.R. Menter, in Proceedings of 24th Fluid Dynamics Conference, July 6-9, 1993, Orlando, FL

[12] B. Mahmoodi, S.H. Hosseini, G. Ahmadi, Particuology. 43 (2019) 171-180

[13] F. Marchelli, Q.F. Hou, B. Bosio, E. Arato, A.B. Yu, Powder Technol. 360 (2020) 1253-1270

[14] V. Salikov, S. Antonyuk, S. Heinrich, V.S. Sutkar, N.G. Deen, J.A.M. Kuipers, Powder Technol. 270 (2015) 622–636

[15] S. Pietsch, S. Heinrich, K. Karpinski, M. Müller, M. Schönherr, F. Kleine, C Powder Technol. 316 (2017) 245–255

[16] P. Breuninger, D. Weis, I. Behrendt, P. Grohn, F. Krull, S. Antonyuk, Particuology 42 (2019) 114-125

[17] Y. Yue, T. Wang, Y. Shen, Powder Technol. 366 (2020) 736-746

[18] M. Ebrahimi, E. Siegmann, D. Prieling, B.J. Glasser, J.G. Khinast, Adv. Powder Technol. (2017)

[19] S. Yang, K. Luo, K. Zhang, K. Qiu, J. Fan, Powder Technol. 272 (2015) 85-99

[20] D. Gidaspow, Multiphase flow and fluidization: Continuum and kinetic theory descriptions, Academic Press, New York, 1994

[21] R. Béttega, C.A. da Rosa, R.G. Corrêa, J.T. Freire, Ind. Eng. Chem. Res. 48 (2009) 11181–11188

[22] C.A. Da Rosa, J.T. Freire, Ind. Eng. Chem. Res. 48 (2009) 7813–7820

[23] F. Wu, J. Zhang, X. Ma, W. Zhou, Adv. Powder Technol. 29 (2018) 1848-1858

[24] C.Y. Wen, Y.H. Yu, Mechanics of Fluidization, Chem. Eng. Prog. Symp. Ser. 62 (1966) 100-111

[25] R. Di Felice, Int. J. Multihase Flow 20 (1994) 153-159

[26] L.W. Rong, K.J. Dong, A.B. Yu, Chem. Eng. Sci. 116 (2014) 508-523

[27] R. Beetstra, M.A. van der Hoef, J.A.M. Kuipers, Fluid Mech. Transp. Phenom. 5 (2007) 489-501

[28] D.L. Koch, R.J. Hill, Anu. Rev. Fluid Mech. 33 (2001) 619–647

[29] Y. He, W. Peng, T. Tang, S. Yan, Y. Zhao, Adv. Powder Technol. 27 (2016) 93-104

[30] Y. Zhang, Y. Zhao, L. Lu, W. Ge, J. Wang, C. Duan, Chem. Eng. Sci. 160 (2017) 106-112

[31] S. Sarkar, M.A. Van Der Hoef, J.A.M. Kuipers, Chem. Eng. Sci. 64 (2009) 2683–2669

[32] F. Cello, A. Di Renzo, F.P. Di Maio, Chem. Eng. Sci. 65 (2010) 3128-3139

[33] S. Tenneti, R. Garg, S. Subramaniam, Int. J. Multiphase Flow 37 (2011) 1072-1092

[34] S.C.R. Dennis, S.N. Singh, D.B. Ingham, J. Fluid Mech. 101 (1980) 257-279

[35] K.B. Mathur, N. Epstein, Spouted Beds, Academic Press, New York, 1974

[36] B.P.B. Hoomans, J.A.M. Kuipers, W.J. Briels, W.P.M. Van Swaaij, Chem. Eng. Sci. 51 (1996) 99-118

[37] Ansys, Chapter 4: Turbulence, ANSYS FLUENT Theory Guid, ANSYS, 2020.

J.N.M. BATISTA
R. BÉTTEGA

Federal University of São Carlos, Department of Chemical Engineering, SP, Brazil

NAUČNI RAD

VREDNOVANJE RAZLIČITIH MATEMATIČKIH MODELA U CFD-DEM SIMULACIJI DINAMIKE KONUSNOG FONTANSKOG SLOJA

Ulazni parametri, empirijski i poluempirijski modeli značajno utiču na odgovore dobijene CFD-DEM simulacijama. U ovom radu je procenjen uticaj tri modela turbulencije, tri uslova rotacije čestica i pet modela otpora na dinamičko ponašanje fluida konusnog fontanskog sloja korišćenog za sušenje zrna sirka. Eksperimentalni podaci o padu pritiska čvrstih materija, visini i obliku fontane korišćeni su za validaciju simulacija. Rezultati su pokazali važnost uključivanja rotacije čestica u model radi aproksimiranja rezultata simuliranih eksperimentalnim ponašanjem. U poređenju sa eksperimentalnim podacima, uzimajući u obzir rotaciju čestica po modelu Denisa i saradnika, odstupanje je bilo 2% za visinu fontane i 9,18% za pad pritiska. Za model bez rotacije čestica odstupanja su iznosila 106,33% i 42,31% za visinu fontane i pad pritiska, redom. Za analizirani slučaj, standardni k-ε model turbulencije pokazao je veće slaganje sa eksperimentalnim podacima. Za procenjene modele otpora, najbolje uklapanje sa eksperimentalnim podacima je dobijen Koh-Hilovim modelom otpora, a zatim modelom Gidaspaua, sa odstupanjima manjim od 10%.

Ključne reči: model otpora, rotacija čestica, model turbulencije, zrna sirka.